*Geophys. J. Int.* (2005) **161,** 662–678 doi: 10.1111/j.1365-246X.2005.02635.x

# Seismic investigation of a bottom simulating reflector and quantification of gas hydrate in the Black Sea

M. Zillmer, E. R. Flueh and J. Petersen

*IfM–GEOMAR, Leibniz-Institute for Marine Sciences, Wischhofstr. 1–3,* D–24148 *Kiel, Germany. E-mail: mzillmer@ifm-geomar.de*

Accepted 2005 February 28. Received 2004 December 6; in original form 2003 December 1

## SUMMARY

A bottom simulating reflector (BSR), which marks the base of the gas hydrate stability zone, has been detected for the first time in seismic data of the Black Sea. The survey area is in the northwestern Black Sea at 44°–45°N and 31.5°–32.5°E. In this paper, seismic wide-angle ocean bottom hydrophone (OBH) and ocean bottom seismometer (OBS) data are investigated with the goal to quantify the gas hydrate and free gas saturation in the sediment. An image of the subsurface is computed from wide-angle data by using Kirchhoff depth migration. The image shows the BSR at 205–270 m depth below the seafloor and six to eight discrete layer boundaries between the seafloor and the BSR. The top of the hydrate layer and the bottom of the gas layer cannot be identified by seismic reflection signals. An analysis of traveltimes and reflection amplitudes leads to 1-D *P*-wave velocity–depth and density–depth models. An average *S*-wave velocity of 160 m $s^{-1}$ between the seafloor and the BSR is determined from the traveltime of the *P* to *S* converted wave. The normal incidence *PP* reflection coefficient at the BSR is −0.11, where the *P*-wave velocity decreases from 1840 to 1475 m $s^{-1}$. Velocities and density are used to compute the porosity and the system bulk modulus as a function of depth. The Gassmann equation for porous media is used to derive explicit formulae for the gas hydrate and free gas saturation, which depend on porosity and on the bulk moduli of the dry and saturated sediment. A gas hydrate saturation–depth profile is obtained, which shows that there is 38 ± 10 per cent hydrate in the pore space at the BSR depth, where the porosity is 57 per cent (OBS 24). This value is derived for the case that the gas hydrate does not cement the sediment grains, a model that is supported by the low *S*-wave velocities. There is 0.9 or 0.1 per cent free gas in the sediment below the BSR, depending on the model for the gas distribution in the sediment. The free gas layer may be more than 100 m thick as a result of a zone of enhanced reflectivity, which can be identified in the subsurface image.

**Key words:** amplitude analysis, Black Sea, bottom simulating reflector, gas hydrate, porous media, wide-angle reflection seismics.



## 1 INTRODUCTION

The multidisciplinary research project ‘Gas Hydrates: Occurence, Stability, Transformation, Dynamics and Biology in the Black Sea’ (GHOSTDABS) was aimed at studying gas hydrates in the Black Sea. Gas hydrates are a solid substance composed of methane and other molecules, which are included in a cage of water molecules (Sloan 1990, 1998). They occur in marine sediments at continental margins under low-temperature and high-pressure conditions (Kvenvolden 1993). The survey area is in the northwestern Black Sea near the Dnieper canyon west of the Crimean peninsula (Fig. 1). Michaelis *et al.* (2002) have shown that the methane in the study area is mainly of biogenic origin. The goal of the active seismic experiments was to image gas hydrate occurrences and to quantify gas accumulations. For this purpose, high-resolution multichannel seismic reflection data and three ocean bottom hydrophone (OBH)/ocean bottom seismometer (OBS) wide-angle profiles were acquired during a cruise with the R/V Professor Logachev in 2001 (see also Lüdmann *et al.* 2004). In 1972, natural gas hydrate was recovered for the first time in the Black Sea and in the Caspian Sea (Yefremova & Zhizchenko 1974). Gas hydrate reflectors have been recognized worldwide since the 1970s (e.g. Markl *et al.* 1970; Shipley *et al.* 1979; White 1979), but so far no bottom simulating reflector (BSR) has been reported from the Black Sea.

OBHs and OBSs record the wavefield at the seafloor for a wide range of incidence angles (Bialas & Flueh 1999; Flueh *et al.* 2002). The data have the potential to reveal information about seismic *P*- and *S*-wave velocities and the density of the sediment layers. OBH/OBS data have been used in gas hydrate research primarily by analysing *P*-wave traveltimes (Spence *et al.* 1995; Hobro *et al.* 1998; Posewang & Mienert

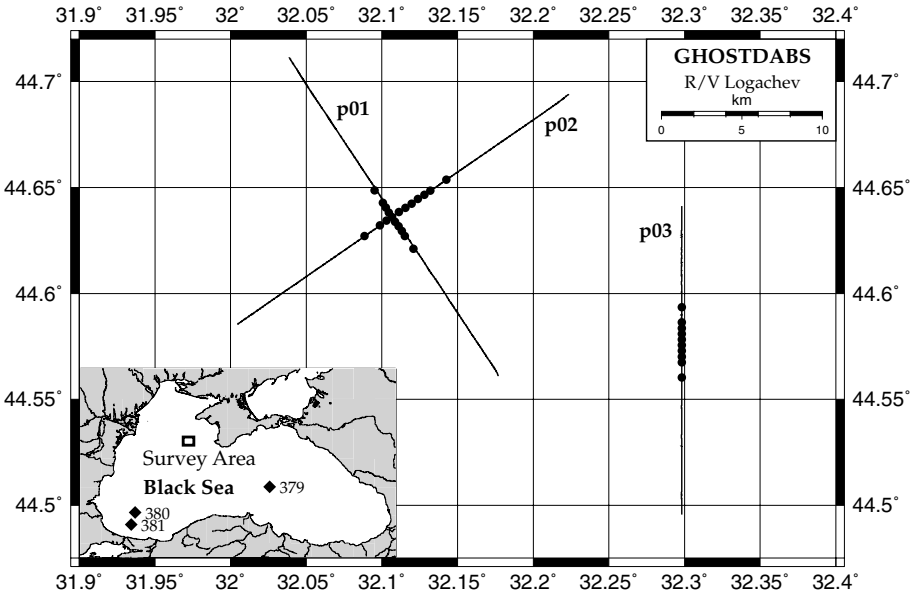


**Figure 1.** Survey area and three OBS profiles in the northwestern Black Sea in 2001. Drill sites 379–381 during DSDP Leg 42B in 1975.

1999; Grevemeyer *et al.* 2000). Tinivella & Accaino (2000) perform traveltime inversion not only on *P*, but also on *S* waves. Korenaga *et al.* (1997) and Holbrook (2001) perform waveform inversion on *P* waves, Katzman *et al.* (1994) interpret traveltimes and amplitudes in OBH data by comparing the data with synthetic seismograms. Tréhu & Flueh (2001) investigate *P*-wave attenuation by analysing amplitudes in OBH data.

*P*-wave amplitudes of the BSR reflection have been investigated in streamer data by using amplitude versus offset (AVO) analysis (Andreassen *et al.* 1995, 1997), synthetic seismogram modeling (Hyndman & Spence 1992; Ecker *et al.* 1998) and waveform inversion (Singh *et al.* 1993; Wood *et al.* 1994; Pecher *et al.* 1998).

Different approaches have been presented in the last decade to connect seismic velocities and density with porosity and gas hydrate saturation (see Chand *et al.* 2004). The theory of wave propagation in porous media (Frenkel 1944; Gassmann 1951; Geertsma & Smit 1961) is one of these methods. Helgerud *et al.* (1999) and Ecker *et al.* (2000) apply the Gassmann equation, and Minshull *et al.* (1994), Tinivella (1999) and Lodolo *et al.* (2002) use the Geertsma–Smit equation.

In this paper, a BSR in the Black Sea is presented in wide-angle data and in the subsurface image, which is obtained from OBH data by Kirchhoff migration. The reflection traveltimes and amplitudes in OBS data are investigated to obtain models for *P*- and *S*-wave velocities and for the density as a function of depth. The Gassmann equation is used to describe wave propagation in gas hydrate and free gas bearing sediments. Explicit formulae for the gas hydrate and the free gas saturation are obtained. The gas hydrate and the free gas saturation are functions of the system bulk modulus, which is determined by analysing the OBH/OBS data. They further depend on porosity and on the dry sediment frame bulk modulus. 1-D models for porosity and hydrate saturation as a function of depth are obtained, and the free gas saturation at the BSR depth is estimated. The errors of the hydrate and free gas saturation estimates are discussed.

## 2 OBH/OBS SEISMIC DATA

The location of the OBS profiles and the survey area in the northwestern Black Sea are shown in Fig. 1. In this paper, we restrict the analysis to profile 3, where a BSR can most clearly be identified (see also Lüdmann *et al.* 2004). The Generator Injector (GI) airgun source radiated acoustic waves with frequencies up to 300 Hz and with the main energy at ∼100 Hz. The distance between the shot points was approximately 14 m. The shot positions were determined with the Global Positioning System and the receiver positions were relocated by using the traveltimes of the direct wave. The recording system operated at a sampling rate of 1 ms and the clock drift during the experiment was taken into account. The OBH/OBS technology is described by Bialas & Flueh (1999) and Flueh *et al.* (2002).

Eight stations (21–25, 27–29) with hydrophones and three-component seismometers were deployed at the seafloor in 1135–1185 m depth, and two hydrophones (26 and 30) were positioned in the water column. The distance between the receivers was 300 m, except for stations 21 and 30, which were deployed at 700 and 900 m distance to the next station. The data of station 29 were lost, as a result of recorder failure. Only three seismometers (OBS 21, 24 and 28) had good coupling to the seafloor, and could be used for the traveltime and amplitude analysis in Section 4. The amplitudes of the direct wave in the hydrophone data are clipped in the near-offset range as a result of overamplification. These data are less suited for an amplitude analysis, in which the direct wave serves as a reference phase. The hydrophone data are used in Section 3 to compute an image of the subsurface.

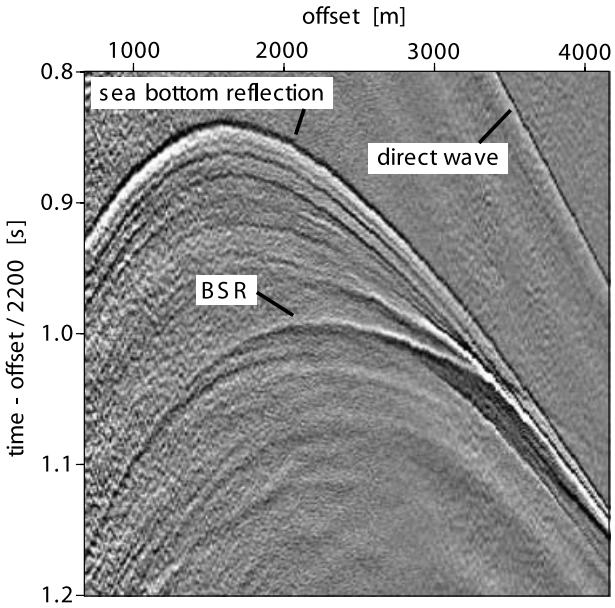


**Figure 2.** The *P* wavefield recorded by the hydrophone of station OBH 26 in the water column 645 m b.s.l. and 529 m a.s.f. The BSR has inverse polarity compared with the direct wave and with the seafloor reflection.

The wavefield measured at OBH 26 is shown in Fig. 2. This hydrophone was suspended in the water column at 645 m below the sea level (b.s.l.) and 529 m above the seafloor (a.s.f.). The raw data show that the BSR has opposite polarity compared with the direct wave and the seafloor reflection. Its traveltime curve cross-cuts the traveltime curves of other sediment reflections.

## 3 KIRCHHOFF DEPTH MIGRATION

Kirchhoff migration transforms the seismogram section in the time domain to an image in space. The Kirchhoff integral is given by (Schneider 1978; Bleistein *et al.* 2001; Zillmer & Kashtan 2004)

$$I(x,z) = \int_{-\infty}^{\infty} w(\xi) u\big(\xi, t = \tau^{(\mathrm{dif})}(x,z)\big)\, d\xi. \tag{1}$$

Here, $I$ denotes the image at the diffraction point $(x, z)$ in the vertical plane through the shot profile. $u$ denotes the seismic data and $\xi$ is a parameter along the shot profile. $w$ denotes a weight function, which compensates for the geometrical spreading loss. $t$ is the time and $\tau^{(\mathrm{dif})}$ is the diffraction traveltime, i.e. the traveltime from the source to the diffraction point plus the traveltime from the diffraction point to the receiver: the data are stacked along diffraction time curves. The traveltimes are computed by seismic ray tracing for a 1-D medium, where *P*-wave velocity is a function of depth. A smooth velocity–depth profile is used to avoid migration artefacts. Correct velocities are determined by iteration, because the wrong migration velocities result in artificially curved reflectors.

An important pre-processing step is to remove the air bubble effect that follows the source signal, i.e. a series of signals with decreasing amplitudes and a period of 0.07 s, which depends on source size and depth. The first of these signals, which follows the direct wave, disturbs the seismic reflections recorded at the seafloor. A time-shift is applied to the hydrophone data, $t \rightarrow t - \tau^{(\mathrm{d})}$, where $\tau^{(\mathrm{d})}$ is the traveltime of the direct wave, and then an $f$–$k$ filter is used to remove the direct wave and the bubble effect. A deconvolution can not be used, because the amplitudes of the direct wave are clipped for small source–receiver offsets.

The data from eight hydrophones are used for migration: OBH 21–25, 27 and 28 at the seafloor and OBH 30 in the water column. OBH 26 is not used because the migrated data have a lower signal-to-noise ratio compared with the other receivers. The Kirchhoff migration is performed using 250 shots to each side of the receiver position. The maximum source–receiver offset of 3.5 km corresponds to 3 times the water depth. The maximum angle of incidence for the *P* wave is 60°–70°, depending on the depth of the reflecting interface. The imaged region is cone shaped, if the layers are horizontal and the propagation velocity is constant. This follows from the geometry of the reflected rays. The seafloor is not imaged by the hydrophones, which are positioned 1 m a.s.f., and horizontal layers, which are close to the seafloor, are only partly imaged.

An image of the sediment layers for profile 3 is shown in Fig. 3. It is composed of the migrated data from eight OBH common receiver gathers. The seafloor and two reflectors within the first 50 m depth below the seafloor (b.s.f.) are imaged by OBH 30 in the water column, and the BSR has inverse polarity compared with the seafloor reflection. A single image extends over a range of 400 m in depth and of up to 350 m laterally to each side of the receiver, depending on depth. There are six to eight layer boundaries between the seafloor and the BSR, which cross-cuts the sediment layers at depths of 205–270 m b.s.f.. The depth of the BSR increases with the water depth according to the pressure–temperature relation at the base of the gas hydrate stability zone (Dickens & Quintby-Hunt 1994). The BSR depth has been used by

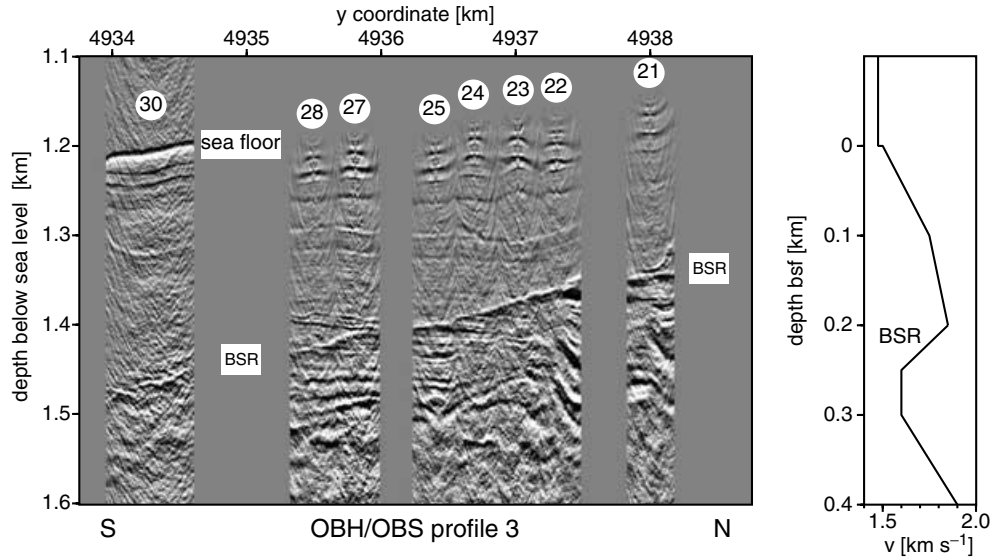


**Figure 3.** The migration image of seismic profile 3 and the 1-D *P*-wave velocity–depth function, which has been used for migrating the hydrophone data, are displayed. Cartesian coordinates are computed by UTM projection (central meridian 33°E) of a WGS84 ellipsoid. The $x$ coordinate of the shot profile is given by $x \approx 444.3$ km. The water depths at the OBS stations are: 1135 m (OBS 21), 1154 m (OBS 22), 1158 m (OBS 23), 1163 m (OBS 24), 1180 m (OBS 25), 1179 m (OBS 27) and 1185 m (OBS 28). OBH 30 is positioned in the water column at 683 m b.s.l. and 518 m a.s.f. The BSR is at 205–270 m depth b.s.f.

Lüdmann *et al.* (2004) to determine the heat flow in the survey area. There is a zone of 100–150 m thickness beneath the BSR with enhanced reflectivity and low velocities, which is interpreted as a zone where free gas is present. The *P*-wave velocity decreases from 1850 to 1600 m $s^{-1}$ at the BSR. The value below the BSR is less reliable than the one above the BSR, because the image in that region is less sensitive to changes in velocities. A *P*-wave velocity of 1475 m $s^{-1}$ is determined from the *PP* reflection coefficient in Section 4.

## 4 ANALYSIS OF THE REFLECTION TRAVELTIMES AND AMPLITUDES

In this section, the reflection traveltimes and amplitudes of the OBS seismogram sections of stations 21, 24 and 28 are analysed in the time domain. The 1-D model of a stack of plane parallel homogeneous layers is used to derive velocity–depth and density–depth functions. A porosity–depth function is computed from the density profile, and bulk and shear modulus functions are computed from the density and from *P*- and *S*-wave velocities. These profiles are used in Section 5 to estimate the gas hydrate and free gas saturation of the sediment.

### 4.1 *P*-wave velocity

Consider a stack of $N$ homogeneous layers, where the first layer is the water layer. The $x$-axis of the coordinate system points along the shot profile and the $z$-axis into depth. A $P$ wave is radiated at the top of layer 1 and propagates through the stack. It is reflected at the interface between layers $N-1$ and $N$, and finally reaches the OBH/OBS receiver at the interface between layers 1 and 2. The traveltime is given by

$$\tau = \sum_{k=1}^{N-1}{}' 2\tau_k = \sum_{k=1}^{N-1}{}' \frac{2h_k}{v_k \cos\theta_k}, \qquad \frac{\sin\theta_1}{v_1} = \frac{\sin\theta_k}{v_k}, \qquad k = 2, 3, \ldots, N-1, \tag{2}$$

where Snell's law is fulfilled at the layer boundaries. The apostrophe means multiplication by $\frac{1}{2}$ for the first layer, because the wave propagates only once through the water layer, but twice through all the sediment layers. $\tau_k$ is the one-way traveltime in layer $k$, $h_k$ is the layer thickness, $v_k$ is the *P*-wave velocity and $\theta_k < \pi/2$ denotes the angle of the ray with the $z$-axis. Eq. (2) is also valid for the direct wave and for the case of an OBH in the water column. A 1-D velocity–depth function is determined from the top to the bottom of the stack. The layer thicknesses are known from the migration image (Fig. 3) and kept constant. Varying the velocity leads to data compatible traveltimes. 350 traces are used, 175 to each side of the OBS position with a maximum offset of 2.5 km. Velocities are determined by trial and error, and accepted if the computed and measured traveltimes deviate by less than 0.004 s for interfaces close to the seafloor and by less than 0.01 s for interfaces close to the BSR. The result for OBS stations 21, 24 and 28 is shown in Fig. 4. The *P*-wave velocity above the BSR is 1840 m $s^{-1}$, which coincides with the result of the depth migration, where a smooth velocity–depth function has been used to avoid migration artefacts. The error increases from approximately $\pm 15$ m $s^{-1}$ at the seafloor to approximately $\pm 50$ m $s^{-1}$ at the BSR.

### 4.2 *S*-wave velocity

The shear waves recorded by the horizontal component of the seismometer at OBS 24 are shown in Fig. 5. The time duration of the *S*-wave signals is much longer than the *P*-wave reflection signals. This low-pass filter effect is characteristic for shear waves in unconsolidated

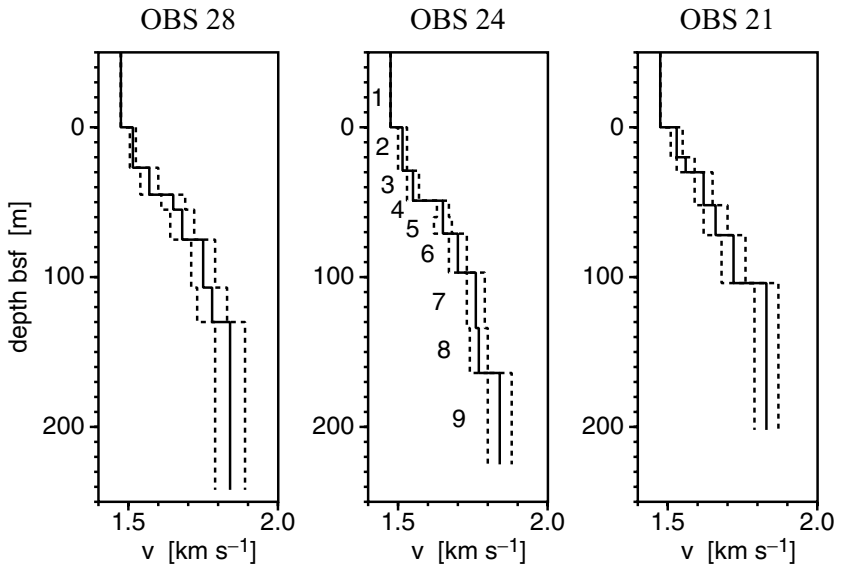


**Figure 4.** *P*-wave velocity above the BSR as a function of depth b.s.f. at OBS stations 21, 24 and 28. The dashed lines are error bounds. Compare the layer numbers at OBS 24 with the reflection coefficients in Fig. 8 below and with the migration image in Fig. 3.

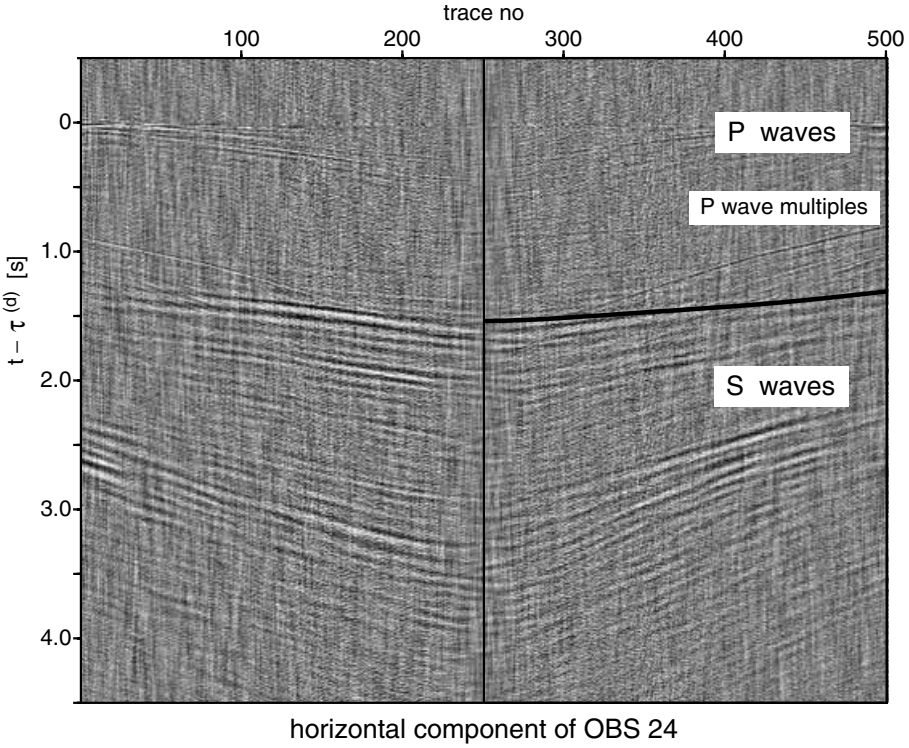


**Figure 5.** Shear and compressional waves recorded with one horizontal component of the seismometer at OBS 24 for 500 shots with a maximum offset of 3.5 km. A time-shift has been applied so that the direct wave arrives at time zero. The traveltime curve for the *P*–*S* converted wave at the BSR is shown (solid line) computed with a constant *S*-wave velocity of 160 m s$^{-1}$ between the seafloor and the BSR.

sediments and is interpreted to be caused by a propagation path of many wavelengths in a medium with a high *S*-wave attenuation. It is not specifically related to the occurrence of gas hydrates. All shear waves are considered to be *P* to *S* converted waves generated during reflection. Theoretically these waves are much larger in amplitude than waves that are converted from *P* to *S* during transmission at the seafloor. The first *S* wave appears at ∼1.6 s after the direct wave. By assuming that the conversion occurs at the BSR, an average *S*-wave velocity of $160 \pm 20$ m s$^{-1}$ is obtained for the depth interval between the seafloor and the BSR. The traveltime curve for this case is plotted in Fig. 5. The empirical relation obtained by Hamilton (1976a) indicates that an increase of the *S*-wave velocity from ∼50 m s$^{-1}$ at the seafloor to ∼350 m s$^{-1}$ at the BSR depth is a more realistic model. Low shear wave velocities do not contribute significantly to the calculation of the

system bulk modulus, which is used in Section 5 to determine the gas hydrate saturation. Because both models lead to similar results for the gas hydrate saturation, the more simple model of a constant *S*-wave velocity is preferred.

### 4.3 *PP* reflection coefficient

*PP* reflection coefficients are derived for all interfaces between the seafloor and the BSR. The reflection amplitudes are investigated in the time domain and reflection coefficients are obtained by normalizing the amplitudes with the shot strength. The shot strength is derived from the amplitude of the direct wave. The radiation pattern and the attenuation in the sediment layers are taken into account, as well as the fact that the receiver is positioned at an interface: the seafloor. The amplitudes are investigated as a function of the incidence angle. Because there is only a onefold coverage of the subsurface, reflections in a common receiver gather are generated at different points laterally on the interface. It is assumed that the lateral changes in reflector properties are small, and that a 1-D model is adequate to derive information about the reflector properties.

A wave that is reflected at the boundary between layer $N-1$ and layer $N$ has the following ray representation in the far field (e.g. Červený & Ravindra 1971):

$$u_3^{(\mathrm{r})}(t) \approx -A\kappa_{N-1,N}\left(\theta_{N-1}^{(\mathrm{r})}\right)\Phi\left(\theta_1^{(\mathrm{r})}\right)L^{-1}\prod_{k=2}^{N-1}T_{k-1,k}^{+}T_{k,k-1}^{-}\cos\theta_1^{(\mathrm{r})}e\left(t-\tau^{(\mathrm{r})}\right). \tag{3}$$

Here, the upper index (r) denotes reflection, $u_3$ is the vertical component of displacement, $A$ is the source amplitude, and $\kappa_{N-1,N}$ is the reflection coefficient for the interface between layers $N-1$ and $N$. $\Phi$ denotes the radiation pattern, and $L$ is the geometrical spreading function. $T_{k-1,k}^{+}$ and $T_{k,k-1}^{-}$ are *P*-wave transmission coefficients for the interface between layers $k-1$ and $k$. The $+$ and $-$ signs indicate that the ray crosses the interface in the positive and negative $z$ direction, respectively. $\cos\,\theta_1^{(\mathrm{r})} > 0$ is the projection of the polarization vector on the $z$-axis and $e$ is the source time function.

The geometrical spreading function $L$ is given by (e.g. Červený & Ravindra 1971)

$$L = \frac{\cos\theta_1^{(\mathrm{r})}}{v_1}\sqrt{\left[\sum_{k=1}^{N-1}{}'\frac{2h_kv_k}{\cos\theta_k^{(\mathrm{r})}}\right]\left[\sum_{k=1}^{N-1}{}'\frac{2h_kv_k}{\cos^3\theta_k^{(\mathrm{r})}}\right]}. \tag{4}$$

The radiation pattern $\Phi$ is caused by the position of the airgun close to the surface of the sea. The airgun represents a centre of pressure source at depth $H$ below a stress-free surface. The point of observation is in the far field at $(r, z)$. The radiated wave is the sum of the direct *P* wave and the *P* wave reflected at the surface with a reflection coefficient of $-1$. An approximation to the radiation pattern is obtained from the phase difference of both waves, assuming a time dependence of the form $e^{+i\omega t}$, where $\omega$ is the frequency and $i$ is the imaginary unit:

$$\exp\left[-\frac{i\omega}{v_1}\sqrt{r^2+(z-H)^2}\right]-\exp\left[-\frac{i\omega}{v_1}\sqrt{r^2+(z+H)^2}\right]\approx\Phi\exp\left[-\frac{i\omega}{v_1}\sqrt{r^2+z^2}\right], \tag{5}$$

where

$$\Phi(\theta)\approx 2i\sin\left(\frac{\omega H}{v_1}\cos\theta\right)\approx i\omega\frac{2H}{v_1}\cos\theta \qquad \text{and} \qquad \cos\theta=\frac{z}{\sqrt{r^2+z^2}}. \tag{6}$$

For the first approximation $H \ll r, z$ has been used and for the second $H \ll \lambda/4$, where $\lambda = 2\pi v_1/\omega$ is the wavelength. If the distance of the centre of pressure source to the free surface is smaller than a quarter wavelength, then the free surface causes a time derivative of the signal, the signal amplitude is proportional to the distance between source and surface and it varies with the cosine of the radiation angle. This approximation is adequate to describe the data: the GI gun was towed during the experiment at a depth of 2–3 m. It generates a signal with a main frequency of ∼100 Hz, which corresponds to a quarter wavelength of approximately 4 m.

By using $f(t) = 2Hv_1^{-1}\dot{e}(t)$, where the dot denotes the time derivative, it follows from eq. (3) for the reflected wave:

$$u_3^{(\mathrm{r})}(t) \approx -A\kappa_{N-1,N}\left(\theta_{N-1}^{(\mathrm{r})}\right)\cos^2\theta_1^{(\mathrm{r})}L^{-1}\prod_{k=2}^{N-1}T_{k-1,k}^{+}T_{k,k-1}^{-}f(t-\tau^{(\mathrm{r})}). \tag{7}$$

The seafloor reflection coefficient is determined with the help of the direct wave, denoted by an upper index (d), and the first multiple in the water column, denoted by an upper index (m). Their ray representations are given by

$$u_3^{(\mathrm{d})}(t) \approx A\frac{h_1^2}{\left(r^2+h_1^2\right)^{3/2}}f\left(t-\tau^{(\mathrm{d})}\right), \qquad \tan\theta_1^{(\mathrm{d})}=\frac{r}{h_1}, \tag{8}$$

and

$$u_3^{(\mathrm{m})}(t) \approx -A\kappa_{1,2}\left(\theta_1^{(\mathrm{m})}\right)\frac{9h_1^2}{\left(r^2+9h_1^2\right)^{3/2}}f\left(t-\tau^{(\mathrm{m})}\right), \qquad \tan\theta_1^{(\mathrm{m})}=\frac{r}{3h_1}. \tag{9}$$

From eqs (8) and (9) follows the seafloor reflection coefficient $\kappa_{1,2}$:

$$\kappa_{1,2}\left(\theta_1^{(\mathrm{m})}\right) \approx -\frac{1}{9}\left(\frac{r^2+9h_1^2}{r^2+h_1^2}\right)^{3/2}\frac{\left[1-\kappa_{1,2}\left(\theta_1^{(\mathrm{d})}\right)\right]U_3(t=\tau^{(\mathrm{m})})}{\left[1-\kappa_{1,2}\left(\theta_1^{(\mathrm{m})}\right)\right]U_3(t=\tau^{(\mathrm{d})})} \approx -\frac{1}{9}\left(\frac{r^2+9h_1^2}{r^2+h_1^2}\right)^{3/2}\frac{U_3(t=\tau^{(\mathrm{m})})}{U_3(t=\tau^{(\mathrm{d})})}, \tag{10}$$

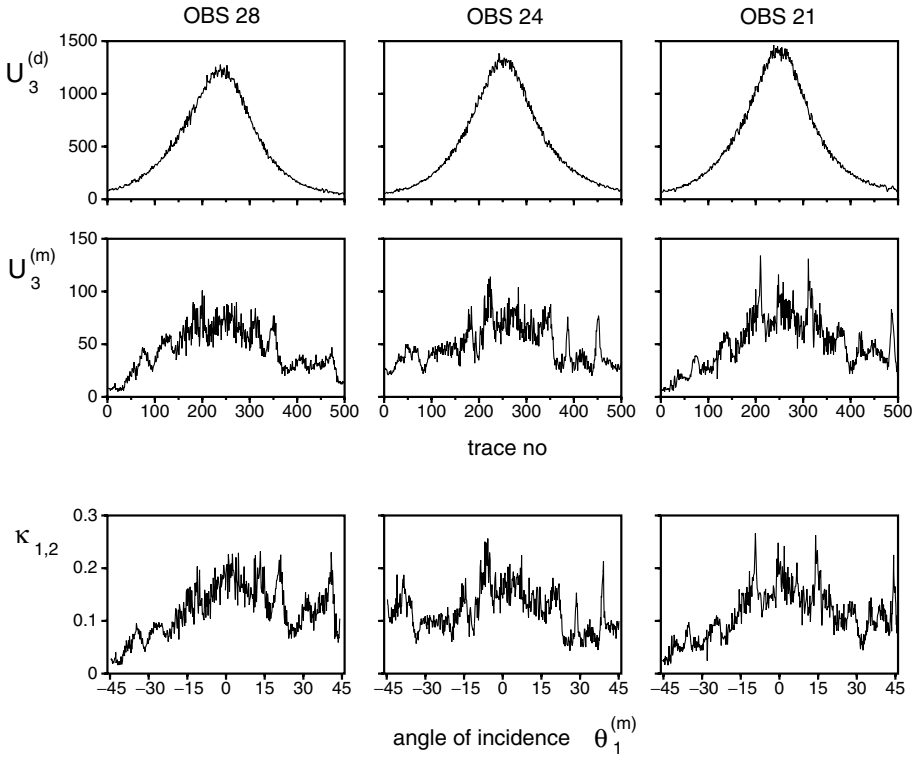


**Figure 6.** The peak-to-peak amplitudes of vertical displacement $U_3$ for the direct wave (d) and the first seafloor multiple (m) recorded in arbitrary units at OBS 21, 24 and 28. The seafloor *P*-wave reflection coefficient $\kappa_{1,2}$ as a function of the incidence angle $\theta_1$.

where $|\kappa_{1,2}| \ll 1$ is used. Here, $U_3$ is the measured vertical component of displacement. The waves are recorded at the seafloor together with the wave, which is reflected back into the water. The source strength $A$ is determined by

$$A \approx \frac{\left(r^2 + h_1^2\right)^{3/2}}{h_1^2} \frac{U_3\left(t = \tau^{(\mathrm{d})}\right)}{1 - \kappa_{1,2}\left(\theta_1^{(\mathrm{d})}\right)}. \tag{11}$$

Peak-to-peak amplitudes are measured in the raw data of OBS stations 21, 24 and 28. The amplitudes of the direct wave and of the first multiple in the water column are displayed in Fig. 6. The amplitude of the seafloor multiple shows very strong scattering, which is caused by local variations in seafloor reflectivity. The *P*-wave reflection coefficient at the seafloor is calculated by eq. (10), leading to ∼0.165 for normal incidence at OBS 24. On average, a decrease of the reflection coefficient with the angle of incidence is observed. The theoretical *P*-wave reflection coefficient for a fluid–solid interface (Ben-Menahem & Singh 2000) indicates that this decrease is caused by a high *S*-wave velocity of ∼400 m s$^{-1}$ in the first few metres b.s.f.. This *S*-wave velocity is attributed to the carbonate crust at the seafloor (Michaelis *et al.* 2002). A shear wave velocity of 160 m s$^{-1}$ derived from the *S*-wave traveltimes is considered to be a more realistic average value for the depth interval between the seafloor and the BSR.

Finally, the *P*-wave reflection coefficient $\kappa_{N-1,N}$ for the interface between layers $N-1$ and $N$ is given by

$$\kappa_{N-1,N}\left(\theta_{N-1}^{(\mathrm{r})}\right) \approx (-)\frac{h_1^2}{\left(r^2 + h_1^2\right)^{3/2}} \frac{1 - \kappa_{1,2}\left(\theta_1^{(\mathrm{d})}\right)}{v_1 \cos\theta_1^{(\mathrm{r})}} \sqrt{\left[\sum_{k=1}^{N-1}{}' \frac{2h_k v_k}{\cos\theta_k^{(\mathrm{r})}}\right]\left[\sum_{k=1}^{N-1}{}' \frac{2h_k v_k}{\cos^3\theta_k^{(\mathrm{r})}}\right]} \prod_{k=2}^{N-1} \left(T_{k-1,k}^{+} T_{k,k-1}^{-}\right)^{-1} \frac{\hat{U}_3(t = \tau^{(\mathrm{r})})}{U_3(t = \tau^{(\mathrm{d})})}, \tag{12}$$

where eqs (4), (7) and (11) have been used. Here, $\hat{U}_3$ is the measured vertical component of displacement, corrected by the attenuation loss in the sediment layers.

The attenuation is described by a frequency independent $Q$ factor, which is calculated recursively by

$$Q_k = \frac{\tau_k^{(\mathrm{r})}}{\gamma_k - \gamma_{k-1}}, \qquad k = 2, 3, \ldots, N-1, \tag{13}$$

where $\gamma_1 = 0$ in the water layer. Here, $\gamma_{N-1}$ denotes the slope of the logarithm of the spectral amplitude ratio of the direct wave and the wave, which is reflected between layers $N-1$ and $N$:

$$\gamma_{N-1} = \frac{\partial}{\partial\omega} \ln \left| \frac{U_3^{(\mathrm{d})}(\omega)}{U_3^{(\mathrm{r})}(\omega)} \right| = \sum_{k=2}^{N-1} \frac{\tau_k^{(\mathrm{r})}}{Q_k}. \tag{14}$$

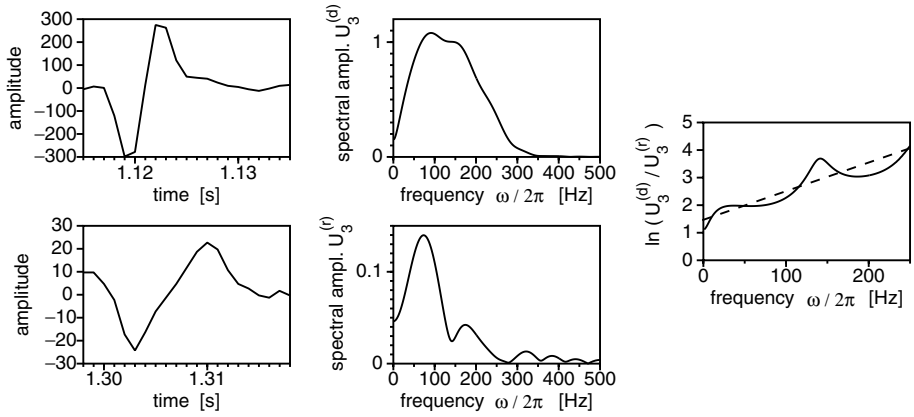


**Figure 7.** Time signal and amplitude spectrum of the direct wave (d) and of the *P*-wave BSR reflection (r) for the vertical component of displacement recorded at OBS station 24 for a single shot. The BSR reflection has the inverse polarity of the direct wave, but it arrives at the seismometer from the opposite direction. The quality factor is approximated by $Q_p \approx (\tau^{(r)} - \tau^{(d)})/\gamma \approx 100$, where $\gamma$ is the slope of the logarithm of the spectral amplitude ratio as a function of $\omega$ (dashed line).

The attenuation loss is compensated in the frequency domain by

$$\hat{U}_3(t) = \frac{1}{\pi}\mathrm{Re}\left\{ \int_0^\infty U_3(\omega)\exp(i\omega t)\exp\left[\omega \sum_{k=2}^{N-1} \frac{\tau_k^{(r)}}{Q_k}\right] d\omega \right\}, \tag{15}$$

where Re denotes the real part of a complex function and $U_3(\omega)$ denotes the spectrum of the seismic data:

$$U_3(\omega) = \int_{-\infty}^{\infty} U_3(t)\exp(-i\omega t)\, dt. \tag{16}$$

The integrand $U_3(\omega)$ in eq. (15) has been set to zero for frequencies above 200 Hz to avoid high frequency noise. Alternatively, the attenuation loss is compensated in the time domain by using

$$\hat{U}_3(t) = U_3(t)\exp\left[\omega_0 \sum_{k=2}^{N-1} \frac{\tau_k^{(r)}}{Q_k}\right], \tag{17}$$

where $\omega_0/2\pi = 100$ Hz is the main frequency of the signal. Both methods were applied and led to similar results. An average value of $Q_p \approx 100$ has been obtained for the *P*-wave attenuation in the sediment layers above the BSR by investigating a few traces recorded at OBS 24 (Fig. 7). A more detailed analysis of attenuation as a function of depth is beyond the scope of the paper. Average $Q_p$ factors of 50 and 200 for the depth interval between the seafloor and the BSR did not significantly change the result for the gas hydrate saturation derived in Section 5.

The *P*-wave velocities, obtained by the traveltime analysis, show that all layer boundaries are weak contrasts. If we assume that the density contrasts are small too, then eq. (12) can be simplified. This assumption is later validated, when the density is determined. In this case, the ray direction does not change significantly at the interface and the geometrical spreading is approximated by the simple formula for a homogeneous medium, i.e. the ray length. Numerical tests have shown that the error is insignificant for angles of incidence smaller than 60°. If the reflected wave crosses each interface from both sides, on its downward and on its upward path, then the following approximation is valid for a weak contrast interface including terms of first order in differences of elastic parameters (Aki & Richards 2002):

$$T^+_{k-1,k}T^-_{k,k-1} \approx 1, \qquad k = 2, 3, \ldots, N-1. \tag{18}$$

Then the following formula is obtained from eq. (12):

$$\kappa_{N-1,N}\left(\theta_{N-1}^{(r)}\right) \approx -\left[1 - \kappa_{1,2}\left(\theta_1^{(d)}\right)\right]\left(\frac{r^2+d^2}{r^2+h_1^2}\right)^{3/2}\left(\frac{h_1}{d}\right)^2 \frac{\hat{U}_3(t=\tau^{(r)})}{U_3(t=\tau^{(d)})} \qquad \text{with} \qquad d = \sum_{k=1}^{N-1}{}'2h_k. \tag{19}$$

The factors on the right-hand side (rhs) have the following meaning: The first factor takes into account that the direct wave is measured at the seafloor together with the wave reflected into the water column. The second factor compensates the effects of spreading loss, polarization and radiation pattern. The reflection amplitude is normalized with help of the direct wave and compensated for the attenuation loss.

Eq. (19) is used to obtain reflection coefficients as a function of incidence angle from the measured vertical component of the OBS data. The coefficients for nine interfaces between the seafloor and the BSR at OBS 24 are shown in Fig. 8. The *f*–*k* filtered data have been used and additionally the raw data for comparison to make sure that there are no filtering effects on the amplitudes. The coefficient for the interface between layers 7 and 8 is not used, because this interface is a thin layer with a positive contrast followed by a negative contrast of the same size, which would lead to a thin layer of reduced gas hydrate saturation. The BSR reflection coefficient takes the value −0.11 for vertical incidence. Except for the first two interfaces, all reflection coefficients are nearly constant for incidence angles in the interval between 0° and 30–45°. In this case, it follows from the *P*-wave reflection coefficient for a weak contrast interface that the contrast in *S*-wave velocity is small (Aki & Richards 2002).

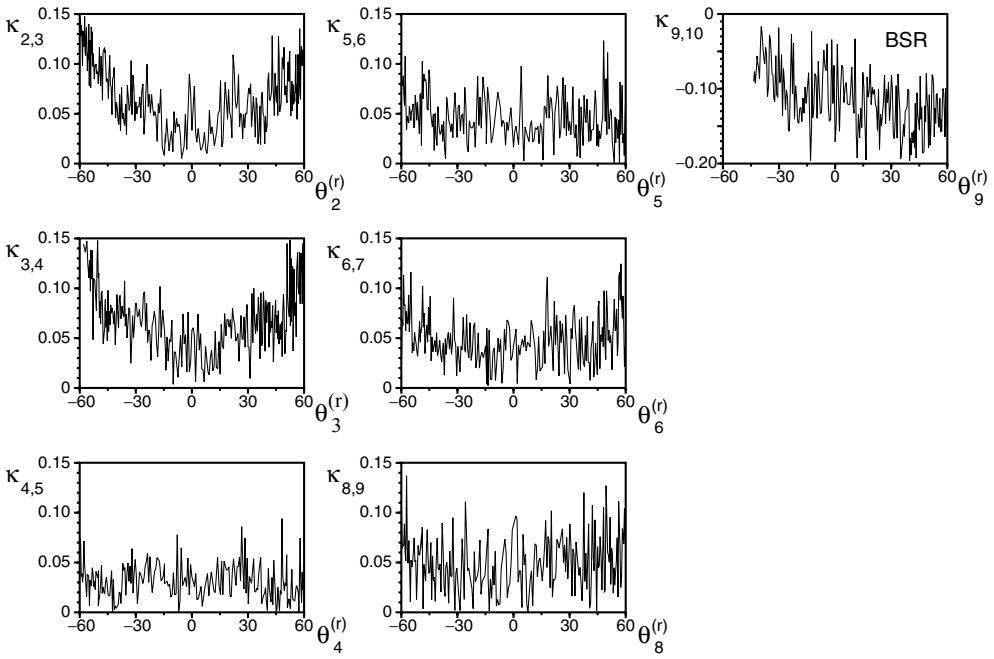


**Figure 8.** *P*-wave reflection coefficients $\kappa_{N-1,N}$ as a function of incidence angles $\theta^{(\mathrm{r})}_{N-1}$ for the interfaces between the seafloor and the BSR at OBS 24. The interface between layers 7 and 8 is not considered (see text). The attenuation loss has been compensated by a $Q_p$ factor of 100 for the depth interval between the seafloor and the BSR.

### 4.4 Density

The reflection coefficient for vertical incidence is given by the impedance contrast between the layers (Aki & Richards 2002):

$$\kappa_{k-1,k}(0) \equiv \kappa_{k-1,k}\left(\theta^{(\mathrm{r})}_{k-1} = 0\right) = \frac{\rho_k v_k - \rho_{k-1} v_{k-1}}{\rho_{k-1} v_{k-1} + \rho_k v_k}, \qquad k = 2, 3, \ldots, N, \tag{20}$$

where $\rho$ is the density. A density–depth profile is computed from the top to the bottom of the stack of layers by using the reflection coefficients and the *P*-wave velocity function:

$$\rho_k = \frac{1 + \kappa_{k-1,k}(0)}{1 - \kappa_{k-1,k}(0)} \frac{\rho_{k-1} v_{k-1}}{v_k}, \qquad k = 2, 3, \ldots, N, \tag{21}$$

where the error is given by

$$\frac{\Delta\rho_k}{\rho_k} = \frac{\Delta\rho_{k-1}}{\rho_{k-1}} + \frac{\Delta v_{k-1}}{v_{k-1}} - \frac{\Delta v_k}{v_k} + \frac{2\Delta\kappa_{k-1,k}(0)}{1 - \kappa^2_{k-1,k}(0)}, \qquad k = 2, 3, \ldots, N. \tag{22}$$

Using $\rho_1 \approx 1.0 \pm 0$ g cm$^{-3}$ for the water layer, the density increases from $1.36 \pm 0.02$ to $1.71 \pm 0.12$ g cm$^{-3}$ between the seafloor and the BSR at OBS 24 (Fig. 9). The error is determined by using the velocity error shown in Fig. 4 and $\Delta\kappa \approx 0.005$ for all layers, which is the

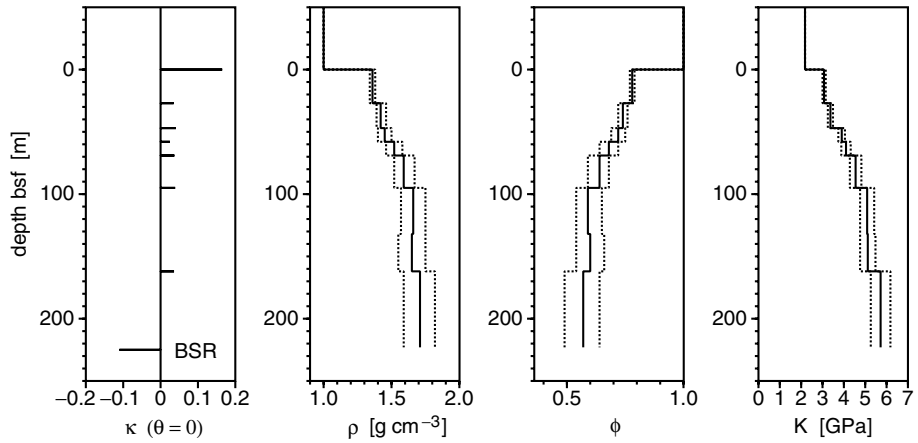


**Figure 9.** *P*-wave reflection coefficient $\kappa$ for vertical incidence ($\theta = 0$), density $\rho$, porosity $\phi$ and system bulk modulus $K$ as a function of depth b.s.f. at OBS station 24 (solid lines). The density is derived from the reflection coefficient, porosity from density, and the bulk modulus from *P*- and *S*-wave velocities and density. The dotted lines are the error bounds.

standard deviation of the reflection coefficient for approximately 60 rays with incidence angles smaller than 20°. Note, that numeric errors quoted above (i.e. ±0.02 and ±0.12) are calculated with eq. (A1).

### 4.5 Porosity

Yuan *et al.* (1996) obtained a reference porosity model from core measurements of a borehole in their survey area, the northern Cascadia slope. There is no borehole in our survey area and the porosity is determined from the density.

The density of gas hydrate bearing sediment is given by the volumetric average of its constituents:

$$\rho = (1-\phi)\rho_s + (\phi - \phi S_h)\rho_w + \phi S_h \rho_h, \tag{23}$$

where $\phi$ is the porosity, $S_h$ is the amount of hydrate in the pore space, $\rho_s$ is the density of the solid phase or grain density, $\rho_w$ is the density of the pore water and $\rho_h$ is the density of gas hydrate. Solving for the porosity leads to

$$\phi = \frac{\rho_s - \rho}{\rho_s - \rho_w + S_h(\rho_w - \rho_h)}. \tag{24}$$

The density of gas hydrate and water are given by $\rho_h \approx 0.91$ g cm$^{-3}$ and $\rho_w \approx 1.0$ g cm$^{-3}$. Gas hydrate and water have similar densities and the amount of hydrate in the pore space is much smaller than 1. The second term $S_h(\rho_w - \rho_h)$ in the denominator of eq. (24) is much smaller than the first term $\rho_s - \rho_w$. Thus, the porosity of the gas hydrate bearing sediment can be approximated by the porosity of the same sediment, when it is fully water saturated:

$$\phi \approx \frac{\rho_s - \rho}{\rho_s - \rho_w}. \tag{25}$$

The porosity error is given by

$$\frac{\Delta\phi}{\phi} \approx \frac{(1-\phi)\Delta\rho_s + \phi\Delta\rho_w - \Delta\rho}{\rho_s - \rho}. \tag{26}$$

The density of gas hydrate samples close to the seafloor has been measured with lower values $\rho_h \approx 0.7$ g cm$^{-3}$, because the samples were porous (Suess *et al.* 2001). Even in this case, eq. (25) is still a useful approximation. Eq. (25) is also used to calculate the porosity in the case of a sediment with free gas, because the amount of gas is usually very small.

For the grain density, a constant value is used for all depths based on information about the mineralogy obtained from DSDP borehole measurements in the Black Sea. In 1975, sediments were recovered by drilling during DSDP Leg 42B of Glomar Challenger. The drill site 379 is located in the central Black Sea, and the sites 380 and 381 are located near the Bosporus (Fig. 1). The sediment consists approximately of 60 per cent clay, 20 per cent quartz and 20 per cent Ca-Mg carbonate on average (Muratov *et al.* 1978). The three constituents have densities $\rho_1 \approx 2.60$ g cm$^{-3}$ (clay), $\rho_2 \approx 2.65$ g cm$^{-3}$ (quartz) and $\rho_3 \approx 2.71$ g cm$^{-3}$ (carbonate; Mavko *et al.* 1998), leading to an average value of $\rho_s \approx 2.63$ g cm$^{-3}$. The precise composition of the sediment in the survey area is unknown and a large error of $\Delta\rho_s = 0.05$ g cm$^{-3}$ is assumed. The error of the density of water is neglected: $\Delta\rho_w \approx 0$. Under these assumptions and using eq. (25) the porosity decreases from 78 ± 1 to 57 ± 7 per cent between the seafloor and the BSR at OBS 24 (Fig. 9). These porosity and density values are close to the empirical function derived by Hamilton (1976b) for terrigenous sediments.

### 4.6 Bulk and shear modulus

The bulk modulus $K$ and the shear modulus $\mu$ of the saturated sediment are determined dynamically with help of the measured density and *P*- and *S*-wave velocities, $v$ and $v_s$.

The shear modulus is given by

$$\mu = \rho v_s^2, \tag{27}$$

where a constant *S*-wave velocity of 160 m s$^{-1}$ is used. The shear modulus increases from 0.03 to 0.05 GPa between the seafloor and the BSR (OBS 24), and the error $\Delta\mu$ can be neglected.

The bulk modulus is given by

$$K = \rho v^2 - \tfrac{4}{3}\mu \tag{28}$$

and its error is approximated by

$$\frac{\Delta K}{K} \approx \frac{\Delta\rho}{\rho} + 2\frac{\Delta v}{v}. \tag{29}$$

The bulk modulus increases from 3.07 ± 0.07 to 5.72 ± 0.46 GPa between the seafloor and the BSR at OBS 24 (Fig. 9).

## 5 ESTIMATION OF GAS HYDRATE AND FREE GAS SATURATION

### 5.1 Gas hydrate saturation

Chand *et al.* (2004) provide a comparison of several methods that have been used to explain the seismic velocities in gas hydrate bearing sediments. In the present study, we use the Gassmann equation to calculate the bulk modulus of the saturated sediment (Frenkel 1944;

Gassmann 1951; Geertsma & Smit 1961; Sheriff & Geldart 1995):

$$K = K^* + \sigma^2 \left( \frac{\phi}{K_\mathrm{f}} + \frac{\sigma - \phi}{K_\mathrm{s}} \right)^{-1}, \qquad \sigma = 1 - \frac{K^*}{K_\mathrm{s}}. \tag{30}$$

Here, $\phi$ is the porosity, $K$, $K^*$, $K_\mathrm{s}$ and $K_\mathrm{f}$ are the bulk moduli of the saturated and the dry sediment, of the solid and of the fluid phase, respectively. The dry sediment bulk modulus is also called the frame or skeleton bulk modulus and the bulk modulus of the saturated sediment is also called the system bulk modulus.

The bulk modulus of the solid phase $K_\mathrm{s}$ is calculated by averaging the bulk moduli of the solid sediment constituents:

$$2K_\mathrm{s} = \sum_i \frac{V_i}{V} K_i + \left( \sum_i \frac{V_i}{V} \frac{1}{K_i} \right)^{-1}, \qquad V = \sum_i V_i. \tag{31}$$

Here, $K_i$ is the bulk modulus of the $i$th constituent, $V_i$ is the volume, which is occupied by the $i$th constituent, and $V$ is the total volume of the solid phase. The precise mineral composition of the sediment in the study area is unknown. DSDP borehole measurements at three locations in the Black Sea (Muratov *et al.* 1978) indicate that the sediment in our survey area could be composed of 60 per cent clay ($K_1 \approx 23$ GPa), 20 per cent quartz ($K_2 \approx 37$ GPa) and 20 per cent Ca-Mg carbonate ($K_3 \approx 71$ GPa). The elastic constants are taken from Mavko *et al.* (1998); eq. (31) leads to $K_\mathrm{s} \approx 32$ GPa and a large error of $\Delta K_\mathrm{s} = 5$ GPa is assumed. With the same mineral composition, a shear modulus of $\mu_\mathrm{s} \approx 16$ GPa is obtained, from which follows $\nu_\mathrm{s} \approx 0.29$ for the Poisson ratio of the solid phase.

Hamilton (1971) derived an empirical formula for the dry sediment bulk modulus, which is given by (compare Guerin *et al.* 1999)

$$K^*(\phi) \approx K_\mathrm{s} 10^{-4.25\phi}. \tag{32}$$

A theoretical method to calculate $K^*$ is described by Mavko *et al.* (1998) and by Dvorkin *et al.* (1999). The bulk modulus $K^*(\phi_\mathrm{c})$ and the shear modulus $\mu^*(\phi_\mathrm{c})$ of an aggregate of spheres under pressure at critical porosity $\phi_\mathrm{c}$ are calculated with the Hertz–Mindlin theory:

$$K^*(\phi_\mathrm{c}) = \left[ \frac{C^2(1-\phi_\mathrm{c})^2}{18\pi^2(1-\nu_\mathrm{s})^2} \right]^{1/3} \mu_\mathrm{s}^{2/3} P^{1/3} \qquad \text{and} \qquad \mu^*(\phi_\mathrm{c}) = \frac{3(5-4\nu_\mathrm{s})}{5(2-\nu_\mathrm{s})} K^*(\phi_\mathrm{c}). \tag{33}$$

The coordination number $C$ (the average number of contacts per sphere) and the critical porosity $\phi_\mathrm{c}$ of a dense random pack of spheres are given by $C \approx 9$ and $\phi_\mathrm{c} \approx 0.36$, respectively. The effective pressure $P$ is the difference between the overburden pressure and the pore pressure:

$$P(z) = \int_0^z g(\rho - \rho_\mathrm{f})\, d\zeta, \tag{34}$$

where $g \approx 9.81$ m s$^{-2}$ is the gravitational acceleration, $z$ is the depth, $\rho$ is the bulk density and $\rho_\mathrm{f}$ is the pore fluid density.

$K^*$ is calculated in the suspension domain, i.e. for $\phi > \phi_\mathrm{c}$, with help of a modified upper Hashin–Shtrikman bound as described in Dvorkin *et al.* (1999),

$$K^*(\phi) = \left\{ \frac{1-\phi}{1-\phi_\mathrm{c}} \left[ K^*(\phi_\mathrm{c}) + \tfrac{4}{3}\mu^*(\phi_\mathrm{c}) \right]^{-1} + \frac{\phi - \phi_\mathrm{c}}{1-\phi_\mathrm{c}} \left[ \tfrac{4}{3}\mu^*(\phi_\mathrm{c}) \right]^{-1} \right\}^{-1} - \tfrac{4}{3}\mu^*(\phi_\mathrm{c}), \tag{35}$$

and in the case of $\phi < \phi_\mathrm{c}$, it is calculated by

$$K^*(\phi) = \left\{ \frac{\phi}{\phi_\mathrm{c}} \left[ K^*(\phi_\mathrm{c}) + \tfrac{4}{3}\mu^*(\phi_\mathrm{c}) \right]^{-1} + \frac{\phi_\mathrm{c} - \phi}{\phi_\mathrm{c}} \left[ K_\mathrm{s} + \tfrac{4}{3}\mu^*(\phi_\mathrm{c}) \right]^{-1} \right\}^{-1} - \tfrac{4}{3}\mu^*(\phi_\mathrm{c}). \tag{36}$$

The second case is not applied here, because the porosities obtained show that the sediment is in the suspension domain (Fig. 9). The empirical relation (32) leads to $K^* \approx 0.13$ GPa at the BSR depth and the model eqs (33–55) to $K^* \approx 0.28$ GPa. Because these values are small, both methods lead to similar results for the gas hydrate saturation (Fig. 10).

By using borehole log measurements from ODP Leg 164 at the Blake-Bahamas ridge offshore South Carolina, Guerin *et al.* (1999) derived an empirical relation $K^*(\phi)$ for gas hydrate bearing sediments for the porosity interval $0.55 < \phi < 0.65$:

$$K^*(\phi) \approx K_\mathrm{s} 10^{3.02 - 7.372\phi}. \tag{37}$$

The resultant calculated dry sediment bulk modulus is more than 20 times higher than the result of Hamilton for sediments without gas hydrate. Guerin *et al.* (1999) use a cementation theory to explain this result, i.e. the gas hydrate cements the grain boundaries. They report that the gas hydrate saturation obtained for the Blake ridge using eq. (37) is consistent with the amount of hydrate recovered from cores of an *in situ* pressure core sampler. A cementation effect has also been observed in laboratory experiments with synthetic gas hydrate bearing sand samples (Best *et al.* 2004).

The Gassmann equation can be used to compute a reference profile for the bulk modulus of a fully water saturated sediment (compare fig. 5 in Guerin *et al.* 1999). If there is gas hydrate/free gas in the sediment, then the measured bulk modulus is larger/smaller than the rhs of eq. (30). In the following, we derive explicit formulae for the gas hydrate and the free gas saturation by using eq. (30), and perform an error estimation.

Gas hydrate in the sediment either reduces the porosity and changes the bulk modulus of the solid phase or it changes the bulk modulus of the pore fluid. These two models have been proposed by Helgerud *et al.* (1999) and by Ecker *et al.* (2000).

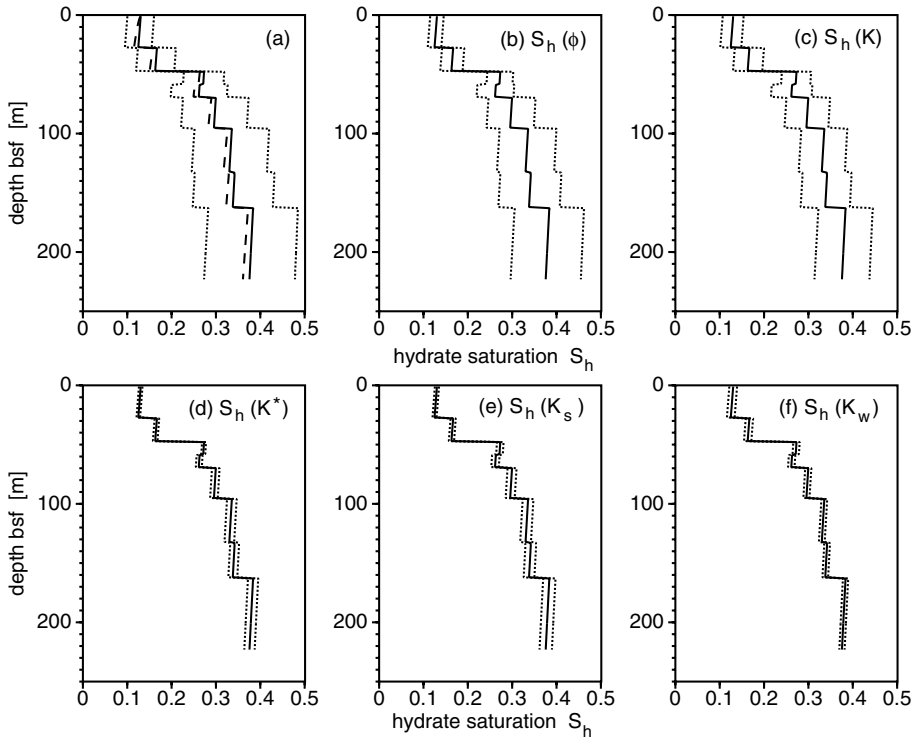


**Figure 10.** (a) Gas hydrate saturation $S_h$ of the pore space as a function of depth b.s.f. between the seafloor and the BSR at OBS 24. $K^*$ is computed by eq. (32) (solid line) or by eqs (33)–(35) (dashed line). The functions $S_h \pm \Delta S_h$ are displayed by dotted lines: (a) for the total error calculated with eq. (A1), and for errors (b) $\Delta\phi$, (c) $\Delta K$, (d) $\Delta K^* = K^*$, (e) $\Delta K_s = 5$ GPa and (f) $\Delta K_w = 0.02$ GPa. The errors of $\phi$ and $K$ are displayed in Fig. 9.

If gas hydrate is a part of the pore fluid, then the bulk modulus is computed with the Reuss average for an isostress system (Mavko *et al.* 1998):

$$\frac{1}{K_f} = \frac{\hat{S}_h}{K_h} + \frac{1-\hat{S}_h}{K_w}. \tag{38}$$

Here, $\hat{S}_h$ is the hydrate saturation of the pore space and $K_h \approx 8.3$ GPa is the bulk modulus of gas hydrate (Helgerud *et al.* 2003). The bulk modulus $K_w$ of the pore water depends on pressure and temperature (Mavko *et al.* 1998). The temperature increases from 9 °C at the seafloor (Lüdmann, private communication, 2004) to 17 °C at the BSR depth of 223 m b.s.f. at OBS 24 and the pressure increases from 11.4 to 14.9 MPa. Then $K_w$ increases from 2.14 to 2.24 GPa, where the error is 0.02 GPa for a temperature error of 2 °C. Substituting eq. (38) into the Gassmann eq. (30) and solving for $\hat{S}_h$ leads to

$$\hat{S}_h = \left(\frac{1}{K_w} - \frac{1}{K_h}\right)^{-1} \left[\frac{1}{K_w} - \frac{1}{K_s} - \frac{\sigma}{\phi}\left(\frac{\sigma}{K-K^*} - \frac{1}{K_s}\right)\right]. \tag{39}$$

If gas hydrate is part of the solid phase, it reduces the porosity. The effective porosity $\overline{\phi} = \phi - \phi S_h$ is substituted for $\phi$ in eq. (30), where $S_h$ is the hydrate saturation of the pore space for this model. This leads to

$$S_h = 1 - \left(\frac{1}{K_w} - \frac{1}{K_s}\right)^{-1} \frac{\sigma}{\phi}\left(\frac{\sigma}{K-K^*} - \frac{1}{K_s}\right), \tag{40}$$

where $K_w$ has been substituted for $K_f$. $K_s$ and $K^*$ on the rhs of this equation are functions of $S_h$. $K_s$ is given by

$$2K_s = \frac{\phi S_h}{1-\overline{\phi}} K_h + \frac{1-\phi}{1-\overline{\phi}} \sum_i \frac{V_i}{V} K_i + \left(\frac{\phi S_h}{1-\overline{\phi}} \frac{1}{K_h} + \frac{1-\phi}{1-\overline{\phi}} \sum_i \frac{V_i}{V} \frac{1}{K_i}\right)^{-1} \tag{41}$$

and $K^*$ is computed with eq. (32) or eqs (33)(– 35) as a function of the effective porosity $\overline{\phi}$ instead of $\phi$. In this case, eq. (40) has to be solved numerically or graphically for $S_h$. If the gas hydrate saturation is small, $S_h \ll 1$, then it follows $\overline{\phi} \approx \phi$. In this case, the rhs of eq. (40) can be considered as independent of $S_h$; it is solved directly and the error is estimated by using the partial derivatives given in Appendix A.

From eqs (39) and (40) it follows:

$$\frac{\hat{S}_h}{S_h} = \frac{K_h(K_s - K_w)}{K_s(K_h - K_w)} \approx \frac{K_h}{K_h - K_w} \approx 1.4, \tag{42}$$

where $K_s \gg K_w$ has been used. Gas hydrate as a part of the pore fluid leads to an ∼1.4 times higher estimates than gas hydrate as a part of the solid phase (compare figs 1 and 2 of Helgerud *et al.* 1999; and fig. 10 of Ecker *et al.* 2000). Ecker *et al.* (1998), Helgerud *et al.* (1999)

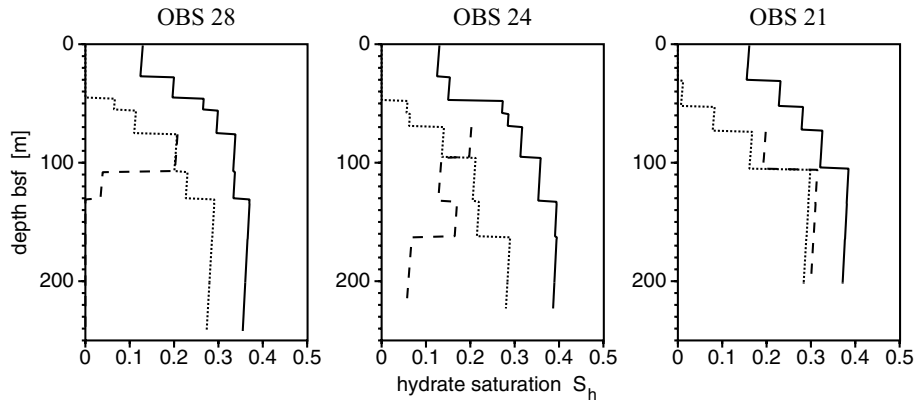


**Figure 11.** Gas hydrate saturation as a function of depth between the seafloor and the BSR at OBS stations 21, 24 and 28. The dry sediment bulk modulus is calculated with eq. (32) (solid line), with eq. (37) (dashed lines) or for a constant value $K^* = 1$ GPa (dotted lines). In the last two cases, the hydrate acts as a cement and increases the bulk modulus of the dry sediment, which leads to much lower gas hydrate saturations.

and Ecker *et al.* (2000) report that the model of gas hydrate as a part of the solid phase leads to estimates for the gas hydrate saturation at the Blake ridge, which are consistent with those obtained from resistivity measurements and from pore water chloride concentrations.

The model of gas hydrate as a part of the solid phase without cementation effect is applied first. The absence of a cementation effect is supported by the observed low *S*-wave velocities. The resultant calculated gas hydrate saturation $S_h$ increases from 13 to 38 per cent of the pore space between the seafloor and the BSR at OBS 24 (Fig. 10). The error bounds show that uncertainties in porosity and system bulk modulus have the largest impact on determining $S_h$. Gas hydrate saturation profiles for OBS 21, 24 and 28 are shown in Fig. 11 (solid lines) with similar results for all stations. The saturation function of Fig. 10 was computed by assuming the rhs of eq. (40) was independent of $S_h$, whereas for Fig. 11 this dependence was taken into account. The difference between the two results is small.

The model, where the gas hydrate cements the sediment grain boundaries, is also investigated. $K^*$ is computed by eq. (37) as function of $\phi$ not $\overline{\phi}$ (Guerin, private communication, 2004). It takes the values 0.9, 2.3 and 2.8 GPa at the BSR depth at OBS stations 21, 24 and 28. These values are obtained via eq. (37) from small differences in porosities (62, 57 and 55 per cent) and they lead to very different gas hydrate saturations (dashed lines in Fig. 11): 30 per cent at OBS 21, 6 per cent at OBS 24 and a negative value at OBS 28. The negative value is physically implausible and, moreover, the BSR can be identified in the migrated section of OBH 28 (Fig. 3). Note, that eq. (37) is an empirical relation that was determined from a single data set at another area and, as such, it is not too surprising that it would not adequately describe a cementation effect for the sediment in our survey area. The cementation theory of Dvorkin *et al.* (1994) can also not be applied to determine $K^*$, because it is valid only for porosities lower than the critical porosity. If a constant dry sediment bulk modulus of 1 GPa is assumed, then the gas hydrate saturation is given by the dotted lines in Fig. 11. There is currently no theoretical support for choosing this larger value for $K^*$, but the fact that gas hydrates were not recovered from the seafloor in the survey area (Lüdmann *et al.* 2004) implies that larger dry sediment bulk moduli (or smaller porosities or larger shear wave speeds, etc.) are needed to drive the predictions of the moduli closer to zero at the seafloor.

Lüdmann *et al.* (2004) obtained gas hydrate saturations of 28 per cent at the BSR, by using the porosity profile of the DSDP borehole 379, and by computing the bulk density from porosity and mineralogy. The borehole is not located in the survey area (Fig. 1). In the present investigation, density, porosity and bulk modulus are directly derived from the seismic data. The borehole logs are only used to estimate the grain density $\rho_s$ and the bulk modulus $K_s$ of the solid phase; large errors of these parameters are allowed and the error discussion shows that they have a relatively minor impact on the calculation of $S_h$. $\rho_s$ and $K_s$ could probably be chosen without additional information from borehole measurements. It is interesting to note that, when assuming $K^* = 1$ GPa, the model with hydrate as a solid phase component also predicts a gas hydrate saturation of approximately 28 per cent just above the BSR (see dotted lines in Fig. 11).

The gas hydrate saturation estimate for our survey area is higher than the results for the Blake ridge offshore South Carolina, which take average values of 5–10 per cent and maximum values around 10–20 per cent (Guerin *et al.* 1999; Helgerud *et al.* 1999; Collett & Ladd 2000; Ecker *et al.* 2000). According to eq. (40), the calculated gas hydrate saturation mainly depends on the factor $\phi(K - K^*)$. The lower gas hydrate saturations at the Blake ridge are related to lower porosities, higher *S*-wave velocities and higher dry sediment bulk moduli $K^*$. For a successful application of eq. (40), it is necessary to obtain *P*- and *S*-wave velocities, porosity and density from seismic or borehole measurements in the survey area.

### 5.2 Free gas saturation

Helgerud *et al.* (1999) propose two alternative models to estimate the free gas content: a patchy distribution of fully gas and fully water saturated sediment, or a homogeneous distribution of gas and water in the pore space.

In the case of a patchy distribution, gas saturated and water saturated sediment occupy neighbouring regions on a length scale much larger than the pore size, but much smaller than the wavelength. The shear modulus is not affected by the elastic properties of the pore fluid

**Table 1.** Parameters to estimate the free gas saturation at OBS 24.

| $\rho$ (g cm$^{-3}$) | $\phi$ | $v$ (m s$^{-1}$) | $v_s$ (m s$^{-1}$) | $K$ (GPa) | $\mu$ (GPa) | $K_s$ (GPa) | $K^*$ (GPa) | $K_w$ (GPa) | $K_g$ (GPa) |
|---|---|---|---|---|---|---|---|---|---|
| $1.71 \pm 0.12$ | $0.57 \pm 0.07$ | $1475 \pm 50$ | $250 \pm 100$ | $3.58 \pm 0.43$ | $0.11 \pm 0.09$ | $32 \pm 5$ | $0.2 \pm 0.1$ | $2.24 \pm 0.02$ | $0.029 \pm 0.001$ |

and equals the shear modulus of the dry sediment (Frenkel 1944; Gassmann 1951). In this case, the inverse *P*-wave modulus is averaged between fully gas and fully water saturated sediment to obtain the *P*-wave modulus of the medium (Hill 1963; Mavko *et al.* 1998). By using eqs (28) and (30) one obtains

$$\left(K + \tfrac{4}{3}\mu\right)^{-1} = S_g \left[ K^* + \tfrac{4}{3}\mu + \sigma^2 \left( \frac{\phi}{K_g} + \frac{\sigma - \phi}{K_s} \right)^{-1} \right]^{-1} + (1 - S_g) \left[ K^* + \tfrac{4}{3}\mu + \sigma^2 \left( \frac{\phi}{K_w} + \frac{\sigma - \phi}{K_s} \right)^{-1} \right]^{-1}. \tag{43}$$

Here, $S_g$ is the part of the pore volume, which is occupied by free gas, and $K_g$ is the adiabatic bulk modulus of the gas. Solving eq. (43) for $S_g$ leads to

$$S_g = \sigma^{-2}\phi^{-1}\left(K + \tfrac{4}{3}\mu\right)^{-1} \left( \frac{1}{K_g} - \frac{1}{K_w} \right)^{-1} \left[ \sigma^2 + (K^* + \tfrac{4}{3}\mu) \left( \frac{\phi}{K_g} + \frac{\sigma - \phi}{K_s} \right) \right] \left[ \sigma^2 - (K - K^*) \left( \frac{\phi}{K_w} + \frac{\sigma - \phi}{K_s} \right) \right]. \tag{44}$$

$K_g$ is determined for methane at a temperature of 17 °C and a hydrostatic pressure of 14.9 MPa (OBS 24) according to the formula in Mavko *et al.* (1998). It is difficult to determine the *P*-wave velocity below the BSR from migration velocity analysis and from ray tracing. Therefore, the velocity is determined from the reflection coefficient assuming that the density does not change at the BSR (compare Section 4.4). The result of 1475 m s$^{-1}$ is considered to be more reliable than the value of 1600 m s$^{-1}$, which has been used to migrate the data below the BSR (Fig. 3). The shear wave velocity is either constant or it increases with depth. Both options were taken into account to arrive at the value for $v_s$ given in Table 1. The gas saturation of the pore space is determined with the parameters of Table 1, which leads to $S_g \approx 0.9 \pm 1.8$ per cent. The error is computed by using eq. (A1) and the partial derivatives of Appendix A. The largest errors are caused by uncertainties of $\phi$(1.1 per cent) and $K$ (1.4 per cent).

In the second model, free gas and water are homogeneously distributed in the pore space. This leads to the same result as for gas hydrate (eq. 39), substituting $K_g$ for $K_h$:

$$\hat{S}_g = \left( \frac{1}{K_w} - \frac{1}{K_g} \right)^{-1} \left[ \frac{1}{K_w} - \frac{1}{K_s} - \frac{\sigma}{\phi} \left( \frac{\sigma}{K - K^*} - \frac{1}{K_s} \right) \right], \tag{45}$$

where $\hat{S}_g$ is the free gas saturation for this model. With the parameters of Table 1, the gas saturation of the pore space is $\hat{S}_g \approx 0.13 \pm 0.25$ per cent at OBS 24 for the homogeneous gas distribution. The largest errors are again caused by uncertainties of $\phi$ (0.17 per cent) and $K$ (0.19 per cent). The error is computed by using the partial derivatives of Appendix A. It is known that for this model a very small amount of gas leads to a strong decrease in *P*-wave velocity (Domenico 1976).

The ratio of the free gas saturation estimated by both models is given by

$$\frac{S_g}{\hat{S}_g} = (K - K^*)\sigma^{-2}\left(K + \tfrac{4}{3}\mu\right)^{-1} \left[ \sigma^2 + (K^* + \tfrac{4}{3}\mu) \left( \frac{\phi}{K_g} + \frac{\sigma - \phi}{K_s} \right) \right]. \tag{46}$$

If $\phi \gg 0$ and $K_g \ll K^* + \frac{4}{3}\mu \ll K \ll K_s$ are used, then follows:

$$\frac{S_g}{\hat{S}_g} \approx 1 + \phi \frac{K^* + \frac{4}{3}\mu}{K_g}, \tag{47}$$

which here is a factor of $\sim$8.

## 6 CONCLUSIONS

A BSR, which marks the base of the gas hydrate stability zone, has been detected for the first time in seismic data from the Black Sea (see also Lüdmann *et al.* 2004). The BSR is identified in 205–270 m depth b.s.f. in the depth migrated seismic section. The top of the gas hydrate layer and the bottom of the gas layer cannot be identified by seismic reflection signals. The enhanced reflectivity beneath the BSR indicates that the zone of free gas is 100–150 m thick.

A method for the quantification of gas hydrate saturation and free gas saturation of the sediment is presented, which is based on measurements of the seismic wavefield with OBSs. The recorded *P*-wave traveltimes and amplitudes and the *S*-wave traveltimes are used to determine the porosity and the system bulk modulus. The Gassmann equation for porous media is used to derive explicit formulae for gas hydrate and free gas saturation. Uncertainties in the saturation estimates are computed as functions of the input variables. The free gas saturation below the gas hydrate layer is $0.9 \pm 1.8$ or $0.13 \pm 0.25$ per cent of the pore space, depending on whether the gas is distributed patchily or homogenously, respectively, in the sediment. The largest uncertainty in the gas hydrate saturation estimate is the result of the unknown dry sediment frame bulk modulus. An empirical formula for cemented dry sediment bulk modulus, determined from another survey area, did not give reliable estimates. A physical model for the dry sediment bulk modulus in high porosity sediments containing gas hydrate as a cement is not available. If gas hydrate does not cement the sediment grains, which is consistent with the low shear wave velocity observed

at the site, but rather acts as a load bearing component of the dry sediment frame, then the hydrate saturation of the pore space at the BSR depth is determined to be 38 ± 10 per cent with most of the uncertainty coming from uncertainties in the measured values of porosity and system bulk modulus. This gas hydrate saturation estimate corresponds to 22 ± 8 per cent of the total sediment volume for a sediment at 57 ± 7 per cent porosity. If the gas hydrate did cement grain contacts, the resultant increase in dry frame bulk modulus combined with the observed system bulk modulus and porosity would lead to a decrease in calculated gas hydrate saturation from the 38 ± 10 per cent reported here.

## ACKNOWLEDGMENTS

The authors are grateful to the reviewers M. Helgerud, G.D. Spence and W.T. Wood for their valuable comments, which helped to improve the manuscript. The GHOSTDABS project was supported by the German Federal Ministry of Education and Research BMBF and the German Research Foundation DFG (project 03G0559D). This is publication no. GEOTECH-120 of the GEOTECHNOLOGIEN program of BMBF and DFG and publication no. 12 of the GHOSTDABS project. The software packages GMT and SU were used in preparing this manuscript.

## REFERENCES

Aki, K. & Richards, P.G., 2002. *Quantitative Seismology,* 2nd edn, University Science Books, Sausalito, CA.

Andreassen, K., Hart, P.E. & Grantz, A., 1995. Seismic studies of a bottom simulating reflection related to gas hydrate beneath the continental margin of the Beaufort Sea, *J. geophys. Res.,* **100,** 12 659–12 673.

Andreassen, K., Hart, P.E. & MacKay, M., 1997. Amplitude versus offset modeling of the bottom simulating reflection associated with submarine gas hydrates, *Mar. Geol.,* **137,** 25–40.

Ben-Menahem, A. & Singh, S.J., 2000. *Seismic Waves and Sources,* 2nd edn, Dover Publications, Mineola, NY.

Best, A.I., Priest, J.A. & Clayton, C.R., 2004. Laboratory seismic measurements on methane gas hydrate bearing sand samples, *Geophys. Res. Abs.,* **6,** EGU04-A-07887.

Bialas, J. & Flueh, E.R., 1999. Ocean bottom seismometers, *Sea Technol.,* **40**(4), 41–46.

Bleistein, N., Cohen, J.K. & Stockwell, J.W., Jr, 2001. *Mathematics of Multidimensional Seismic Imaging, Migration, and Inversion,* Springer Verlag, New York.

Červený, V. & Ravindra, R., 1971. *Theory of seismic head waves,* University of Toronto Press, Toronto.

Chand, S., Minshull, T.A., Gei, D. & Carcione, J.M., 2004. Elastic velocity models for gas-hydrate-bearing sediments—a comparison, *Geophys. J. Int.,* **159,** 573–590.

Collett, T.S. & Ladd, J., 2000. Detection of gas hydrate with downhole logs and assessment of gas hydrate concentrations (saturations) and gas volumes on the Blake Ridge with electrical resistivity log data. In: Paull, C.K. *et al.* (eds), *Proc. ODP, Sci. Results, 164,* pp. 179–191, Ocean Drilling Program, College Station, TX.

Dickens, G.R. & Quintby-Hunt, M.S., 1994. Methane hydrate stability in seawater, *Geophys. Res. Lett.,* **21,** 2115–2118.

Domenico, S.N., 1976. Effect of brine-gas mixture on velocity in an unconsolidated sand reservoir, *Geophysics,* **41,** 882–894.

Dvorkin, J., Nur, A. & Yin, H., 1994. Effective properties of cemented granular material, *Mech. Mater.,* **18,** 351–366.

Dvorkin, J., Prasad, M., Sakai, A. & Lavoie, D., 1999. Elasticity of marine sediments: Rock physics modeling, *Geophys. Res. Lett.,* **26,** 1781–1784.

Ecker, C., Dvorkin, J. & Nur, A., 1998. Sediments with gas hydrates: Internal structure from seismic AVO, *Geophysics,* **63,** 1659–1669.

Ecker, C., Dvorkin, J. & Nur, A.M., 2000. Estimating the amount of gas hydrate and free gas from marine seismic data, *Geophysics,* **65,** 565–573.

Flueh, E.R., Klaeschen, D. & Bialas, J., 2002. Options for multi-component seismic data aquisition in deep water, *First Break,* **20,** 764–769.

Frenkel, J., 1944. On the theory of seismic and seismoelectric phenomena in a moist soil, *J. Phys. USSR,* **8,** 230–241.

Gassmann, F., 1951. Über die Elastizität poröser Medien, *Vierteljahrsschrift der Naturforschenden Gesellschaft in Zürich,* **96,** 1–23.

Geertsma, J. & Smit, D.C., 1961. Some aspects of elastic wave propagation in fluid-saturated porous solids, *Geophysics,* **26,** 169–181.

Grevemeyer, I, Rosenberger, A. & Villinger, H., 2000. Natural gas hydrates on the continental slope off Pakistan: constraints from seismic techniques, *Geophys. J. Int.,* **140,** 295–310.

Guerin, G., Goldberg, D. & Meltser, A., 1999. Characterization of in situ elastic properties of gas hydrate–bearing sediments on the Blake Ridge, *J. geophys. Res.,* **104,** 17 781–17 795.

Hamilton, E.L., 1971. Elastic properties of marine sediments, *J. geophys. Res.,* **76,** 579–604.

Hamilton, E.L., 1976a. Shear–wave velocity versus depth in marine sediments: a review, *Geophysics,* **41,** 985–996.

Hamilton, E.L., 1976b. Variations of density and porosity with depth in deep-sea sediments, *J. Sediment. Petrol.,* **46,** 280–300.

Helgerud, M.B., Dvorkin, J., Nur, A., Sakai, A. & Collett, T., 1999. Elastic-wave velocity in marine sediments with gas hydrate: Effective medium modeling, *Geophys. Res. Lett.,* **26,** 2021–2024.

Helgerud, M.B., Waite, W.F., Kirby, S.H. & Nur, A., 2003. Measured temperature and pressure dependence of $v_p$ and $v_s$ in compacted, polycrystalline sI methane and sII methane-ethane hydrate, *Can. J. Phys.,* **81,** 47–53.

Hill, R., 1963. Elastic properties of reinforced solids: Some theoretical principles, *J. Mech. Phys. Solids,* **11,** 357–372.

Hobro, J.W., Minshull, T.A. & Singh, S.C., 1998. Tomographic seismic studies of the methane hydrate stability zone in the Cascadia Margin, in, *Gas Hydrates: Relevance to World Margin Stability and Climate Change,* Special Publication 137, pp. 133–140, eds Henriet, J.-P. & Mienert, J., Geological Society, London.

Holbrook, W.S., 2001. Seismic studies of the Blake Ridge: Implications for hydrate distribution, methane expulsion, and free gas dynamics, *Am. geophys. Un. Monogr.,* **124,** 235–256.

Hyndman, R.D. & Spence, G.D., 1992. A seismic study of methane hydrate marine bottom simulating reflectors, *J. geophys. Res.,* **97,** 6683–6698.

Katzman, R., Holbrook, W.S. & Paull, C.K., 1994. Combined vertical–incidence and wide-angle seismic study of a gas hydrate zone, Blake Ridge, *J. geophys. Res.,* **99,** 17 975–17 995.

Korenaga, J., Holbrook, W.S., Singh, S.C. & Minshull, T.A., 1997. Natural gas hydrates on the southeast U.S. margin: Constraints from full waveform and traveltime inversions of wide-angle seismic data, *J. geophys. Res.,* **102,** 15 345–15 365.

Kvenvolden, K.A., 1993. Gas hydrates—Geological perspective and global change, *Rev. Geophys.,* **31,** 173–187.

Lodolo, E., Camerlenghi, A., Madrussani, G., Tinivella, U. & Rossi, G., 2002. Assessment of gas hydrate and free gas distribution on the South Shetland margin (Antartica) based on multichannel seismic reflection data, *Geophys. J. Int.,* **148,** 103–119.

Lüdmann, T., Wong, H.K., Konerding, P., Zillmer, M., Petersen, J. & Flueh, E.R., 2004. Heat flow and quantity of methane deduced from a gas hydrate field in the vicinity of the Dnieper Canyon, northwestern Black Sea, *Geo-Mar. Lett.,* **24,** 182–193, DOI: 10.1007/s00367-004-0169-y.

Markl, R.G., Bryan, G.M. & Ewing, J.I., 1970. Structure of the Blake–Bahama Outer Ridge, *J. geophys. Res.,* **75,** 4539–4555.

Mavko, G., Mukerij, T. & Dvorkin, J., 1998. *The rock physics handbook,* Cambridge University Press, Cambridge.

Michaelis, W. *et al.*, 2002. Microbial reefs in the Black Sea fueled by anaerobic oxidation of methane, *Science,* **297,** 1013–1015.

Minshull, T.A., Singh, S.C. & Westbrook, G.K., 1994. Seismic velocity structure at a gas hydrate reflector, offshore western Colombia, from full waveform inversion, *J. geophys. Res.,* **99,** 4715–4734.

Muratov, M.V., Neprochonov, Y.P., Ross, D.A. & Trimonis, E.S., 1978. Basic features of the Black Sea late cenozoic history based on the results of deep-sea drilling, Leg 42B, in *Initial Reports of the Deep Sea Drilling Project,* Vol. 42, Part 2, pp. 1141–1148, eds Ross, D.A. *et al.*, US Government Printing Office, Washington.

Pecher, I.A., Ranero, C.R., von Huene, R., Minshull, T.A. & Singh, S.C., 1998. The nature and distribution of bottom simulating reflectors at the Costa Rican convergent margin, *Geophys. J. Int.,* **133,** 219–229.

Posewang, J. & Mienert, J., 1999. High-resolution seismic studies of gas hydrates west of Svalbard, *Geo-Mar. Lett.,* **19,** 150–156.

Schneider, W.A., 1978. Integral formulation for migration in two and three dimensions, *Geophysics,* **43,** 49–76.

Sheriff, R.E. & Geldart, L.P., 1995. *Exploration seismology,* 2nd edn, Cambridge University Press, Cambridge.

Shipley, T.H., Houston, M.H., Buffler, R.T., Shaub, F.J., McMillen, K.J., Ladd, J.W. & Worzel, J.L., 1979. Seismic evidence of widespread possible gas hydrate horizons on continental slopes and rises, *Am. Assoc. Petrol. Geol. Bull.,* **63,** 2204–2213.

Singh, S.C., Minshull, T.A. & Spence, G.D., 1993. Velocity structure of a gas hydrate reflector, *Science,* **260,** 204–207.

Sloan, E.D., Jr, 1990. *Clathrate hydrates of natural gases,* Marcel Dekker, New York.

Sloan, E.D., Jr, 1998. Physical/chemical properties of gas hydrates and application to world margin stability and climatic change, in *Gas Hydrates: Relevance to World Margin Stability and Climate Change,* Special Publication 137, pp. 31–50, eds Henriet, J.-P. & Mienert, J., Geological Society, London.

Spence, G.D., Minshull, T.A. & Fink, C., 1995. Seismic studies of methane gas hydrate, offshore Vancouver Island. In: Carson, B. *et al.* (eds), *Proc. ODP, Scientific Results, 146,* Part 1, pp. 163–174, Ocean Drilling Program, College Station, TX.

Suess, E. *et al.*, 2001. Sea floor methane hydrates at Hydrate Ridge, Cascadia Margin, *Am. geophys. Un. Monogr.,* **124,** 87–98.

Tinivella, U., 1999. A method for estimating gas hydrate and free gas concentrations in marine sediments, *Bollettino di Geofisica Teorica ed Applicata,* **40,** 19–30.

Tinivella, U. & Accaino, F., 2000. Compressional velocity structure and Poisson's ratio in marine sediments with gas hydrate and free gas by inversion of reflected and refracted seismic data (South Shetland Islands, Antartica), *Mar. Geol.,* **164,** 13–27.

Tréhu, A.M. & Flueh, E.R., 2001. Estimating the thickness of the free gas zone beneath Hydrate Ridge, Oregon continental margin, from seismic velocities and attenuation, *J. geophys. Res.,* **106,** 2035–2045.

White, R.S., 1979. Gas hydrate layers trapping free gas in the Gulf of Oman, *Earth planet. Sci. Lett.,* **42,** 114–120.

Wood, W.T., Stoffa, P.L. & Shipley, T.H., 1994. Quantitative detection of methane hydrate through high-resolution seismic velocity analysis, *J. geophys. Res.,* **99,** 9681–9695.

Yefremova, A.G. & Zhizchenko, B.P., 1974. Occurrence of crystal hydrates of gases in the sediments of modern marine basins, *Akademii Nauk SSSR,* **214,** 1179–1181.

Yuan, T., Hyndman, R.D., Spence, G.D. & Desmons, B., 1996. Seismic velocity increase and deep-sea gas hydrate concentration above a bottom-simulating reflector on the northern Cascadia continental slope, *J. geophys. Res.,* **101,** 13 655–13 671.

Zillmer, M. & Kashtan, B.M., 2004. True amplitude migration of reflection seismic data from the KTB site, *Geophys. Res. Abs.,* **6,** EGU04-A-03494.

## APPENDIX A: PARTIAL DERIVATIVES OF THE FORMULAE FOR THE GAS HYDRATE AND FREE GAS SATURATIONS

The error $\Delta y$ of the function $y(x_1, x_2, \ldots, x_n)$ is calculated by

$$\Delta y = \sqrt{\sum_{i=1}^{n} \left( \frac{\partial y}{\partial x_i} \Delta x_i \right)^2}, \tag{A1}$$

where $\Delta x_i$ is the error of the variable $x_i$.

The error of the gas hydrate saturation $S_h$ (eq. 40) can be determined with the help of the following partial derivatives:

$$\frac{\partial S_h}{\partial \phi} = \frac{1 - S_h}{\phi}, \tag{A2}$$

$$\frac{\partial S_h}{\partial K} = \left( \frac{1}{K_w} - \frac{1}{K_s} \right)^{-1} \frac{\sigma^2}{\phi (K - K^*)^2}, \tag{A3}$$

$$\frac{\partial S_h}{\partial K^*} = -\left( \frac{1}{K_w} - \frac{1}{K_s} \right)^{-1} \phi^{-1} \left[ \frac{\sigma}{K - K^*} \left( \frac{\sigma}{K - K^*} - \frac{2}{K_s} \right) + \frac{1}{K_s^2} \right], \tag{A4}$$

$$\frac{\partial S_h}{\partial K_w} = \left( \frac{1}{K_w} - \frac{1}{K_s} \right)^{-1} \frac{S_h - 1}{K_w^2}, \tag{A5}$$

$$\frac{\partial S_h}{\partial K_s} = \left( \frac{1}{K_w} - \frac{1}{K_s} \right)^{-1} K_s^{-2} \left[ 1 - S_h + \phi^{-1} \left( 1 - \frac{2\sigma K}{K - K^*} \right) \right]. \tag{A6}$$

The error of the free gas saturation $S_g$ (eq. 44) can be estimated by using the following partial derivatives:

$$\frac{\partial S_g}{\partial \phi} = f_0 \left[ -\frac{1}{\phi} f_1 f_4 - (K - K^*) \left( \frac{1}{K_w} - \frac{1}{K_s} \right) f_1 + \left( K^* + \tfrac{4}{3}\mu \right) \left( \frac{1}{K_g} - \frac{1}{K_s} \right) f_4 \right], \tag{A7}$$

$$\frac{\partial S_g}{\partial K} = -f_0 \left( K + \tfrac{4}{3}\mu \right)^{-1} f_1 f_2, \tag{A8}$$

$$\frac{\partial S_g}{\partial \mu} = -\tfrac{4}{3} f_0 \left(K + \tfrac{4}{3}\mu\right)^{-1} f_3 f_4, \tag{A9}$$

$$\frac{\partial S_g}{\partial K_w} = -f_0 \left(\frac{1}{K_g} - \frac{1}{K_w}\right)^{-1} K_w^{-2} f_1 f_3, \tag{A10}$$

$$\frac{\partial S_g}{\partial K_g} = f_0 \left(\frac{1}{K_g} - \frac{1}{K_w}\right)^{-1} K_g^{-2} f_2 f_4, \tag{A11}$$

$$\frac{\partial S_g}{\partial K^*} = f_0 \left[\frac{2}{\sigma K_s} f_1 f_4 + f_1 \left(\frac{\phi}{K_w} - \frac{\sigma+\phi}{K_s} + \frac{K-K^*}{K_s^2}\right) + f_4 \left(\frac{\phi}{K_g} - \frac{\sigma+\phi}{K_s} - \frac{K^* + \frac{4}{3}\mu}{K_s^2}\right)\right], \tag{A12}$$

$$\frac{\partial S_g}{\partial K_s} = f_0 K_s^{-2} \left\{ -\frac{2K^*}{\sigma} f_1 f_4 + f_1 \left[2\sigma K - (1+\phi)(K-K^*)\right] + f_4 \left[(1+\phi)\left(K^* + \tfrac{4}{3}\mu\right) - \tfrac{8}{3}\sigma\mu\right]\right\}, \tag{A13}$$

where

$$f_0 = \sigma^{-2}\phi^{-1}\left(K + \tfrac{4}{3}\mu\right)^{-1}\left(\frac{1}{K_g} - \frac{1}{K_w}\right)^{-1}, \tag{A14}$$

$$f_1 = \sigma^2 + \left(K^* + \tfrac{4}{3}\mu\right)\left(\frac{\phi}{K_g} + \frac{\sigma-\phi}{K_s}\right), \tag{A15}$$

$$f_2 = \sigma^2 + \left(K^* + \tfrac{4}{3}\mu\right)\left(\frac{\phi}{K_w} + \frac{\sigma-\phi}{K_s}\right), \tag{A16}$$

$$f_3 = \sigma^2 - (K-K^*)\left(\frac{\phi}{K_g} + \frac{\sigma-\phi}{K_s}\right), \tag{A17}$$

$$f_4 = \sigma^2 - (K-K^*)\left(\frac{\phi}{K_w} + \frac{\sigma-\phi}{K_s}\right). \tag{A18}$$

The error of the free gas saturation $\hat{S}_g$ (eq. 45) can be calculated by using the following partial derivatives:

$$\frac{\partial \hat{S}_g}{\partial \phi} = \left(\frac{1}{K_w} - \frac{1}{K_g}\right)^{-1} \frac{\sigma}{\phi^2}\left(\frac{\sigma}{K-K^*} - \frac{1}{K_s}\right), \tag{A19}$$

$$\frac{\partial \hat{S}_g}{\partial K} = \left(\frac{1}{K_w} - \frac{1}{K_g}\right)^{-1} \frac{\sigma^2}{\phi(K-K^*)^2}, \tag{A20}$$

$$\frac{\partial \hat{S}_g}{\partial K^*} = -\left(\frac{1}{K_w} - \frac{1}{K_g}\right)^{-1} \phi^{-1}\left[\frac{\sigma}{K-K^*}\left(\frac{\sigma}{K-K^*} - \frac{2}{K_s}\right) + \frac{1}{K_s^2}\right], \tag{A21}$$

$$\frac{\partial \hat{S}_g}{\partial K_w} = \left(\frac{1}{K_w} - \frac{1}{K_g}\right)^{-1} \frac{\hat{S}_g - 1}{K_w^2}, \tag{A22}$$

$$\frac{\partial \hat{S}_g}{\partial K_s} = \left(\frac{1}{K_w} - \frac{1}{K_g}\right)^{-1} K_s^{-2}\left[1 + \phi^{-1}\left(1 - \frac{2\sigma K}{K-K^*}\right)\right], \tag{A23}$$

$$\frac{\partial \hat{S}_g}{\partial K_g} = -\left(\frac{1}{K_w} - \frac{1}{K_g}\right)^{-1} \frac{\hat{S}_g}{K_g^2}. \tag{A24}$$